

Effect of Bed Clay on Surface Water-Wave Reconstruction from Ripples

Jonathan Malarkey¹, Ellen M. Pollard², Roberto Fernández³, Xuxu Wu^{2,4}, Jaco H. Baas¹
and Daniel R. Parsons⁵

¹School of Ocean Sciences, Bangor University, Menai Bridge, Anglesey LL59 5AB, UK.

²Energy and Environment Institute, University of Hull, Hull, HU6 7RX, UK.

³Department of Civil and Environmental Engineering, The Pennsylvania State University, State College, PA 16802, USA.

⁴School of Environmental Sciences, University of Hull, Hull, HU6 7RX, UK.

⁵Department of Geography and Environment, Loughborough University, Loughborough, LE11 3TU, UK.

Corresponding author: Jonathan Malarkey (j.malarkey@bangor.ac.uk)

Key Points:

- Wave-ripple dimensions provide important information on past subaqueous environments
- Here, a clean-sand method is adapted for clay-sand mixtures by incorporating the effect of changes in the threshold of motion and dimensions
- Clay can result in a reduction in the range of past water-surface wavelengths and water depths, which is largest for coarse sand

18 **Abstract**

19 Wave ripples can provide valuable information on their formative hydrodynamic conditions in
20 past subaqueous environments by inverting dimension predictors. However, these inversions do
21 not usually take the mixed non-cohesive and cohesive nature of sediment beds into account.
22 Recent experiments involving sand–kaolinite mixtures have demonstrated that wave-ripple
23 dimensions and the threshold of motion are affected by bed clay content. Here, a clean-sand
24 method to determine wave climate based on orbital ripple wavelength has been adapted to
25 include the effect of clay and a consistent shear-stress threshold parameterisation. Based on
26 present-day examples with known wave conditions, the results show that the largest clay effect
27 occurs for coarse sand with median grain diameters over 0.45 mm. For a 7.4% volumetric clay
28 concentration, the range of possible water-surface wavelengths and water depths can be reduced
29 significantly, by a factor of three and four, respectively, compared to clean sand.

30 **Plain Language Summary**

31 In shallow water, ripples form on the seabed under water-surface waves due to friction.
32 Knowledge of this process allows preserved ripples to be used to infer past environmental
33 conditions. Traditionally, the method of inferring past environments from wave ripples has only
34 involved sand, despite mixtures of sand and sticky mud being more common in nature. Based on
35 the results of recent mixed sand–mud experiments, the effect of including small amounts of mud
36 in the analysis is shown to be an important modifying factor in determining past environments.

37 **1 Introduction**

38 Bed-surface structures in sediments and sedimentary rocks of past subaqueous
39 environments provide important information on flow hydraulics (e.g. Collinson & Mountney,
40 2019). These structures tend to be classified on the basis of the presence or absence of cohesion
41 in equivalent modern environments: (a) cohesive structures, associated with physical cohesion by
42 clay particles and biological cohesion by extracellular polymeric substances (e.g. biofilms,
43 Vignaga et al., 2013), where the bed is stabilised by cohesion between grains and sudden
44 catastrophic failure may occur under high bed shear stress, e.g. during storms; and (b) non-
45 cohesive bedforms (e.g. wave and current ripples: Wiberg & Harris, 1994; Baas, 1994), where
46 grains can move individually and tend to respond more rapidly and continuously to changes in
47 flow forcing (Perron et al., 2018). Examples of these types of bed-surface structure include roll-
48 ups (Cuadrado, 2020) and non-cohesive wave ripples (e.g. Allen, 1981). Davies (2016) argued
49 that the distinction between cohesive and non-cohesive sedimentary structures is artificial, as
50 they represent end members of a spectrum, and thus predictions based on one classification may
51 result in misinterpretations. This position is re-enforced by recent experiments that have shown
52 how sandy bedforms can be affected by small amounts of biological and physical cohesion
53 (Malarkey et al., 2015; Parsons et al., 2016; Wu et al., 2018; 2022). The consequence for wave
54 ripples of physical cohesion associated with kaolin clay in the bed has been detailed by Wu et al.
55 (2024). Building on the work of Allen (1981), Diem (1985) developed a clean-sand analytical
56 method for the prediction of paleowave climate based on the dimensional measurement of wave
57 ripples in the rock record (Aspler et al., 1994; Wetzel et al., 2003; Allen & Hoffman, 2005;
58 Pochat & Van Den Driessche, 2011, Lamb et al., 2012). Here, Diem's (1985) approach is
59 adapted for sand–clay mixtures, using the synthesis proposed by Wu et al. (2024).

60 Diem's (1985) approach starts by determining the wave orbital diameter from the ripple
 61 wavelength, without requiring a specific wavelength predictor. Here, the formulation starts as
 62 Diem (1985) did, with linear wave theory and additional constraints based on threshold of
 63 motion and wave breaking. It will then return to the effect of clay on ripple-wavelength
 64 prediction and the threshold of motion. The importance of clay content is demonstrated with the
 65 use of present-day examples from the laboratory and field, where the wave conditions were
 66 known.

67 **2 Diem's (1985) method**

68 2.1 Linear wave theory

69 In linear wave theory, the dispersion relation and the wave-velocity amplitude, U_0 , are

$$\sigma^2 = gk \tanh kh, \quad U_0 = \pi d_0 / T, \quad (1a,b)$$

70 where $\sigma = 2\pi/T$, T is the wave period, g is the acceleration due to gravity ($= 9.81 \text{ m s}^{-2}$), $k = 2\pi/L$,
 71 L is the water-surface wavelength, h is the water depth, d_0 is the orbital diameter ($= H/\sinh kh$)
 72 and H is the wave height. The wave properties, characterised by eqs. (1a,b), are subject to two
 73 constraints:

74 2.1.1 Threshold of motion

75 U_t , the critical wave-velocity amplitude associated with the threshold of motion, is a function of
 76 d_0 and D_{50} , the median grain diameter. For sediment movement $U_0^2 > U_t^2$, which when combined
 77 with eqs. (1a,b) gives

$$x < \tanh kh, \quad (2)$$

78 where $x = L/L_{t\infty}$ and $L_{t\infty} = 1/2\pi g(d_0/U_t)^2$ is the deep-water surface wavelength corresponding to the
 79 threshold of motion.

80 2.1.2 Wave breaking

81 According to Miche (1944), the wave-breaking criterion defines the maximum possible wave
 82 steepness as, $H/L \leq 0.142 \tanh kh$, which when combined with d_0 and $L_{t\infty}$ gives

$$x \geq A \cosh kh, \quad (3)$$

83 where $A = d_0/0.142L_{t\infty} = U_t^2/(0.071\pi g d_0)$. It will be shown below that $A < 1/2$, so if $A =$
 84 $1/2(U_t/U_m)^2$, where $U_m = (0.0355\pi g d_0)^{1/2}$ is the maximum wave-velocity amplitude ($U_m > U_t$), then
 85 $U_t < U_0 \leq U_m$ and from eq. (1b) $\pi d_0/U_m \leq T < \pi d_0/U_t$.

86 Eqs. (2) and (3) represent the range of possible conditions between threshold and wave breaking
 87 for the wave climate. The limits of these constraints can be found by combining eqs. (2) and (3)
 88 using the identity $1 - \tanh^2 kh = \text{sech}^2 kh$, such that the maximum and minimum in x satisfy the
 89 equation $x^4 - x^2 + A^2 = 0$, so that $x_{\max, \min}$ are

$$x_{\max, \min} = [1/2 \pm 1/2(1 - 4A^2)^{1/2}]^{1/2}, \quad (4)$$

90 where $A < 1/2$, for there to be two distinct values. Here, x and kh are in the ranges $x_{\min} \leq x < x_{\max}$
 91 and $\arctanh x < kh \leq \operatorname{arccosh}(x/A)$, respectively.

92 Figure 1 shows kh versus x for the limiting single-value case where $U_m^2 = U_t^2$ ($A = 1/2$, $x = 2^{-1/2}$
 93 and $kh = \arctanh 2^{-1/2} \sim 0.88$) from shallow water ($kh \ll 1$) to deep water ($kh \gg 1$). Figure 1 also
 94 shows the $A = 1/4$ case ($U_m^2 = 2U_t^2$), corresponding to typical above-threshold wave conditions. In
 95 the latter case, the shaded region in Figure 1 shows the allowable values of x ($1/4 \cosh kh \leq x <$
 96 $\tanh kh$) and the dots mark $x_{\max, \min} = 1/2(2 \pm 3^{1/2})^{1/2}$ and $kh_{\max, \min} = \arctanh(x_{\max, \min})$. The breaking-
 97 wave curves ($x = A \cosh kh$) are concave downward and the threshold curve ($x = \tanh kh$) is
 98 concave upward. Notice for the breaking-wave curves, $x \rightarrow A$ for $kh \ll 1$ and A also controls the
 99 slope for larger kh . In dimensional terms, the water-surface wavelength, L , is therefore limited by
 100 the threshold scale ($L_{t\infty}$) and breaking-wave scale ($AL_{t\infty}$) according to $AL_{t\infty} < L \leq L_{t\infty}$. Then, from
 101 eqs. (2) and (3), the range of h can be expressed as a function of L as

$$(L/2\pi)\arctanh(L/L_{t\infty}) \leq h \leq (L/2\pi)\operatorname{arccosh}(L/AL_{t\infty}). \quad (5)$$

102 2.2 The ripple predictor

103 Diem's (1985) central assumption is that the orbital diameter can be expressed in terms of an
 104 equilibrium ripple wavelength, λ_e , as

$$\lambda_e = \alpha_0 d_0, \quad (6)$$

105 where $\alpha_0 = 0.65$, based on Miller and Komar's (1980) experiments, provided that $\lambda_e < 200$ mm
 106 ($d_0 = 308$ mm). Above this limit, Diem (1985) proposed the use of Sleath's (1975) predictor.
 107 This arbitrary 200-mm limit represents the lower boundary of the suborbital and anorbital ranges,
 108 where the wavelength is dependent on both d_0 and D_{50} for suborbital ripples and only dependent
 109 on D_{50} for anorbital ripples. However, while a value of α_0 in the range $0.5 \leq \alpha_0 \leq 0.75$ in eq. (6) is
 110 widely accepted, there is little agreement in the literature on the precise nature of the orbital,
 111 suborbital, and anorbital limits. Wiberg and Harris (1994) defined orbital, suborbital and
 112 anorbital ripples by $d_0/D_{50} \leq 1754$, $1754 < d_0/D_{50} \leq 5587$ and $d_0/D_{50} > 5587$, respectively
 113 (Malarkey & Davies, 2003), whereas Mogridge et al. (1994) and Pedocchi and García (2009)
 114 argued the anorbital limit should have wave-period dependence. Provided that eq. (6) *does* hold,
 115 which is what will be assumed here, all quantities involving d_0 can now be expressed in terms of
 116 λ_e .

117 3 Adaptions to Diem's (1985) method

118 3.1 Threshold of motion parameterisation

119 Based on Soulsby's (1997) critical threshold of motion for clean sand, Appendix A derives an
 120 expression for U_t^2 , eq. (A2), such that U_t^2 , $L_{t\infty}$ and $AL_{t\infty}$ can be written

$$U_t^2 = B(gd_0^{0.52}D_{50}^{0.48}), \quad L_{t\infty} = \frac{\pi}{2B} \left(\frac{d_0^{1.48}}{D_{50}^{0.48}} \right), \quad AL_{t\infty} = \frac{d_0}{0.142}, \quad (7a,b,c)$$

121 where $B = 3.653(s-1)\theta_0$, s is the relative density of sediment in water (eq. A1), θ_0 is the critical
 122 skin friction Shields parameter (eq. A1), and $d_0 = \lambda_e/\alpha_0$ from eq. (6). Diem (1985) used Komar
 123 and Miller's (1973) mobility threshold prescription. Here, Soulsby's expression has been used,
 124 as it allows U_t^2 to be directly related to θ_0 and it avoids the need for two different functional
 125 forms, for $D_{50} < 0.5$ mm and $D_{50} \geq 0.5$ mm (eqs. (B1) and (B2)).

126 3.2 Inclusion of the effect of clay

127 Wu et al. (2024) showed that the ratio of wavelength to orbital diameter, α , which replaces α_0 in
128 eq. (6), can be expressed as

$$\alpha = \alpha_0 \times \begin{cases} 1, & C_0 \leq C_{0m}, \\ 1 - 5.5(C_0 - C_{0m}), & C_0 > C_{0m}, \end{cases} \quad (8)$$

129 where α_0 is the clean-sand constant of proportionality (= 0.61), C_0 is the clay content in the bed
130 and $C_{0m} = 7.4\%$ is the minimum value of C_0 where α can change from α_0 , and $\alpha = \frac{1}{2}\alpha_0$ for $C_0 =$
131 16.3% . Whitehouse et al. (2000) showed that the threshold of motion is enhanced by the clay
132 content according to

$$\theta_{0E} = \theta_0 B_\theta, \quad (9)$$

133 where θ_0 is the clean-sand threshold, $B_\theta = 1 + P_\theta C_0$ and P_θ is a constant that depends on the
134 sediment properties. Based on their experiments, Wu et al. (2024) determined that $P_\theta = 6.3$ for
135 $D_{50} = 0.143$ mm and $P_\theta = 23$ for $0.45 \leq D_{50} \leq 0.5$ mm (between these two ranges, it will be
136 assumed that P_θ can be linearly interpolated). Notice in eq. (9) that even small amounts of clay
137 produce an enhancement which is strongly dependent on grain size.

138 Thus, the two main effects of including clay are that α is reduced and θ_{0E} is increased.
139 Substituting eqs. (8) and (9), into eqs. (7a,b,c) gives U_t^2 , $L_{t\infty}$ and $AL_{t\infty}$ as

$$U_t^2 = B \left[\frac{B_\theta}{\alpha^{0.52}} \right] (g\lambda_e^{0.52} D_{50}^{0.48}), \quad L_{t\infty} = \frac{\pi}{2B[B_\theta \alpha^{1.48}]} \left(\frac{\lambda_e^{1.48}}{D_{50}^{0.48}} \right), \quad AL_{t\infty} = \frac{\lambda_e}{0.142[\alpha]}, \quad (10a,b,c)$$

140 where λ_e is the mixed clay–sand ripple wavelength and only the square-bracketed quantity in
141 each expression depends on C_0 .

142 3.3 The method

143 The method begins with the determination of the ripple wavelength, λ_e , and bed-clay content, C_0 .
144 Once these have been determined, the following calculations are undertaken:

145 (i) Use λ_e and C_0 in eqs. (10a,b,c), with α and B_θ given by eqs. (8) and (9), to determine U_t , $L_{t\infty}$
146 and $AL_{t\infty}$

147 (ii) Use A in eq. (4) to determine $x_{\max,\min}$, so that $x_{\min} \leq x \leq x_{\max}$

148 (iii) Use $L = L_{t\infty} x$ to determine the range of h based on eq. (5) and U_t and $U_m = (0.0355\pi g\lambda_e/\alpha)^{1/2}$
149 to determine the ranges of U_0 and T : $U_t < U_0 < U_m$ and $\pi\lambda_e/\alpha U_m < T < \pi\lambda_e/\alpha U_t$

150 4 Example cases

151 With specific examples from the rock record, Diem (1985) was able to show how local
152 considerations and context could be used to further limit the theoretical ranges described in the
153 previous section. Here, modern-day examples, where the wave properties are known, are used, so
154 that attention can be focussed on the effect of clay on the theoretical ranges alone. The example
155 cases correspond to clean, coarse-, medium- and fine-grained sand from the laboratory and field,
156 and involve determining how wave conditions based on the measured ripples change if the clay
157 content is varied in the range $0 \leq C_0 \leq 16.3\%$.

158 4.1 Wu et al. (2018), coarse-sand laboratory data

159 Wu et al. (2018) conducted a series of experiments involving a single-wave condition over a bed
 160 composed of well-sorted coarse sand, $D_{50} = 0.496$ mm ($\theta_0 = 0.032$), and varying clay content, $0 \leq$
 161 $C_0 \leq 7.4\%$. For the clean sand experiment ($C_0 = 0\%$), the wave conditions were given by $h = 0.6$
 162 m, $H = 0.16$ m and $T = 2.49$ s ($L = 5.62$ m), corresponding to $d_0 = 0.223$ m. This experiment
 163 produced ripples with a wavelength $\lambda_e = 278D_{50}$ (Wu et al., 2024). Figure 2a show the threshold
 164 and wave-breaking scales, $L_{T\infty}$ and $AL_{T\infty}$, versus C_0 . $L_{T\infty}$, which is smallest at $C_0 = 7.4\%$, has a
 165 much larger range than $AL_{T\infty}$, which is constant for $C_0 \leq 7.4\%$ and then doubles up to $C_0 =$
 166 16.3% . Figure 2d shows the corresponding L - h phase space, based on eq. (5), for the clay
 167 contents depicted in Figure 2a ($C_0 = 0, 7.4$ and 16.3%). Compared to the dimensionless x - kh plot
 168 (Figure 1), the threshold curves are still concave downwards, but more exaggerated, and the
 169 breaking-wave curves are close to straight lines. The change in ranges is largely due to changes
 170 in $L_{T\infty}$. The reduction in range between the largest and smallest (corresponding to $C_0 = 0\%$ and
 171 7.4%) is by a factor of 3 and 4 for the water-surface wavelength and water depth, respectively
 172 (Figure 2d). Notice that the actual surface wavelength and water depth ($L = 5.62$ m, $h = 0.6$ m)
 173 are within all three ranges. Figures 2a,d can be compared with Figures B1a,b to see the effect of
 174 using the Komar and Miller (1973) clean-sand mobility description for the threshold. This shows
 175 $L_{T\infty}$ to be about 63% of its value in Figure 2a, because $B = 0.21(s-1) = 0.34$ as opposed to
 176 $3.653(s-1)\theta_0 = 0.19$. Thus, using Diem's (1985) clean-sand mobility description underpredicts
 177 the range of water-surface wavelengths and heights in an absolute sense. In a relative sense, the
 178 change in the ranges of clay content is similar, because the powers of d_0 and D_{50} are similar (eq.
 179 (B2), for $D_{50} < 0.5$ mm, and eq. (10a)), but this will not be the case for $D_{50} > 0.5$ mm. Also, the
 180 measured L and h are not within the $C_0 = 7.4\%$ range (Figure B1b). As L and h are below the
 181 threshold curve, this would imply that ripples of this size are relict for this clay content. This is
 182 inconsistent with the experimental results, since Wu et al. (2024) showed no reduction in λ_e for
 183 $C_0 \leq 7.4\%$.

184 4.2 Doucette (2000), medium-sand field data

185 Doucette's (2000) field measurements were taken on a microtidal beach of Wambro Sound (run
 186 1) where $h = 0.47$ m, $H = 0.2$ m and $T = 5.6$ s ($L = 11.9$ m), corresponding to $d_0 = 0.79$ m. The
 187 bed was composed of medium sand, with $D_{50} = 0.22$ mm ($\theta_0 = 0.045$), and the measured ripples
 188 had a wavelength of $\lambda_e = 250$ mm. Since $d_0/D_{50} = 3591$, the ripples were in the suborbital range
 189 (see section 2.2), where the wavelength is dependent on both the orbital and grain diameters.
 190 Notice this wavelength is above Diem's (1985) 200-mm limit. The supporting information
 191 demonstrates that, whilst using Sleath's (1975) predictor for $C_0 = 0$ produces a difference, it is
 192 similar to the other two example cases, which are below Diem's (1985) limit, and so is not
 193 considered significant. From interpolation, P_θ in eq. (9) is determined to be 10. Figure 2b shows
 194 $L_{T\infty}$ and $AL_{T\infty}$ versus C_0 and Figure 2e shows the L - h phase space, for $C_0 = 0, 7.4$ and 16.3% .
 195 These reveal similar behaviour to that of the coarse-grained sand case, but less extreme: in
 196 Figure 2b, $L_{T\infty}$ is still at its minimum at $C_0 = 7.4\%$ and $AL_{T\infty}$ shows the same enhancement as in
 197 Figure 2a. The reduction in range between the largest and smallest ($C_0 = 0\%$ and 7.4%) is by a
 198 factor of 2 for both the water-surface wavelength and water depth (Figure 2e). Again, the actual
 199 surface wavelength and water depth ($L = 11.9$ m, $h = 0.47$ m) are within all three ranges.

200 4.3 Boyd et al. (1988), fine-sand field data

201 Boyd et al.'s (1988) field measurements were undertaken about 1 km from Martinique Beach on
 202 the Atlantic coast of Nova Scotia during a period of relative calm (day 167, hour 9) where $h = 10$

203 m, $H = 0.5$ m and $T = 6.2$ s ($L = 50.7$ m), corresponding to $d_0 = 0.32$ m. The bed was composed
 204 of well-sorted fine sand, with $D_{50} = 0.11$ mm ($\theta_0 = 0.076$), and the measured ripples had a
 205 wavelength of $\lambda_e = 180$ mm. $d_0/D_{50} = 2873$ puts the ripples into the suborbital range. Assuming
 206 that P_θ in eq. (9) is the same as for 0.143 mm ($P_\theta = 6.3$), Figure 2c shows $L_{T\infty}$ and $AL_{T\infty}$ versus C_0
 207 and Figure 2f shows the $L-h$ phase space, for $C_0 = 0, 7.4$ and 16.3%. $L_{T\infty}$ in Figure 2c is still at its
 208 minimum at $C_0 = 7.4\%$, but, because of far weaker clay enhancement of the threshold for fine
 209 sands in eq. (9), $L_{T\infty}$ is largest for $C_0 = 16.3\%$. In Figure 2f, the measured water-surface
 210 wavelength and water depth ($L = 50.7$ m, $h = 10$ m) are below the threshold curve and outside
 211 the range for the $C_0 = 0$ and 7.4% clay contents, and just above the threshold curve and within
 212 range for $C_0 = 16.3\%$, because, unlike the previous cases, $C_0 = 16.3\%$ produces the largest $L_{T\infty}$.
 213 Since there was little clay at the field site, the wave conditions were probably below threshold,
 214 implying that the observed ripples were relict. This is supported by the fact that Boyd et al.'s
 215 (1988) previous observation at day 167, hour 3, showed the same wavelength and no ripple
 216 migration. The reduction in range between the largest and smallest ($C_0 = 16.3\%$ and 7.4%) is
 217 again by a factor of 2 for both the water-surface wavelength and water depth (Figure 2f).

218 5 Discussion

219 The range of L shown in Figure 2 is largely controlled by $L_{T\infty}$, so it is of interest to determine
 220 how the change in clay content affects $L_{T\infty}$, eq. (10b), compared to the original clean-sand Diem
 221 method using Komar and Miller (1973), $L_{T\infty\text{KM}}$, eq. (B2) with $C_0 = 0\%$. The net effect is shown as
 222 a ratio in Figure 3 for $C_0 = 0, 7.4$ and 16.3% and $0.1 \leq D_{50} \leq 0.8$ mm, for the approximate limits
 223 in the range of λ_e/D_{50} of 250 and 1,000. There are two competing effects: the reduction because
 224 of clay content (Figure 2) and the increase because of using Soulsby's (1997) threshold condition
 225 rather than Komar and Miller's (1973). Figure 3 shows a discontinuity for clean sand at $D_{50} = 0.5$
 226 mm as a result of eq. (B2), leading to the largest difference ($L_{T\infty}$ is increased by up to 161% for
 227 $\lambda_e/D_{50} = 250$), which decreases with increasing λ_e/D_{50} (although Diem's (1985) method has
 228 rarely been applied for $D_{50} > 0.5$ mm). Otherwise for $D_{50} \leq 0.19$ mm, $L_{T\infty}$ is reduced by up to
 229 36%, and for $0.19 < D_{50} \leq 0.5$ mm, $L_{T\infty}$ is increased by up to 64%. For $C_0 = 7.4\%$, $L_{T\infty}$ is
 230 consistently decreased by between 35 and 56%, and for $C_0 = 16.3\%$, $L_{T\infty}$ varies only slightly
 231 (increased by up to 14%, for $0.12 \leq D_{50} \leq 0.37$ mm, and otherwise reduced by up to 15%). The
 232 absence of a discontinuity in the present formulation, compared to Diem's (1985) original
 233 formulation, is clearly preferable. Also, the net effect of the clay on $L_{T\infty}$ will be stronger for
 234 smaller than for larger clay contents.

235 It is important to clarify how a representative clay content, C_0 , for the ripples should be
 236 determined. In the modern environment this usually involves measuring C_0 below the active
 237 layer (below trough level), as efficient winnowing often removes clay from the body of the
 238 ripples during development (Wu et al., 2022). In the geological record, clay content in deposits
 239 should be based on primary clay minerals and diagenetic alterations for which it can be
 240 established that the original mineral was part of the primary clay fraction.

241 6 Conclusions

242 Preserved sedimentary bedforms provide important information for reconstructing past
 243 hydraulics in subaqueous environments by inverting bedform predictors, but this is usually based
 244 exclusively on non-cohesive sand. The present work incorporates the effects of sand-clay
 245 mixtures on bedforms, using the experimental results of Wu et al. (2024) in the non-cohesive

246 inversion method of Diem (1985). Based on wave breaking and threshold of motion limitations,
 247 Diem's (1985) approach results in ranges for wave conditions. Here we have shown that the
 248 inclusion of as little as 7.4% clay in the most extreme case of coarse sand, $D_{50} \geq 0.45$ mm,
 249 reduces the possible ranges of water-surface wavelengths and water depths by factors of 3 and 4,
 250 respectively. For fine sand, the ranges are reduced by a factor of two. In short, not accounting for
 251 the modifying effect of clay in ripple growth and equilibrium geometries, may lead to
 252 underestimating the prevailing flow conditions if clay is present.

253 **Appendix A: Determination of U_t^2 based on Soulsby (1997)**

254 According to Soulsby (1997), the Shields parameter for the critical threshold of motion of clean
 255 sand is

$$\theta_0 = \frac{0.3}{1+1.2D_*} + 0.055(1-e^{-0.02D_*}), \quad (\text{A1})$$

256 where $D_* = [(s-1)g/v^2]^{1/3} D_{50}$, $s = \rho_s/\rho$, ρ_s and ρ are the water and sediment densities and v is the
 257 kinematic viscosity ($\sim 1 \text{ mm}^2 \text{ s}^{-1}$). For waves, $\theta_0 = f_w U_t^2 / 2(s-1)gD_{50}$, where $f_w = 1.39(6d_0/D_{50})^{-0.52}$
 258 is the skin friction factor (Soulsby et al., 1993). Rearranging the θ_0 wave expression gives U_t^2 as

$$U_t^2 = B(gd_0^{0.52} D_{50}^{0.48}), \quad (\text{A2})$$

259 where $B = 6^{0.52}(s-1)\theta_0/0.695 = 3.653(s-1)\theta_0$. Eq. (A2) can be compared with eq. (B1).

260 **Appendix B: Diem's (1985) threshold of motion constraint**

261 Diem (1985) used the Komar & Miller (1973) expression for U_t^2 , namely

$$U_t^2 = (s-1)g \times \begin{cases} 0.21(d_0^{0.5} D_{50}^{0.5}), & D_{50} < 0.5 \text{ mm}, \\ 0.46\pi(d_0^{0.25} D_{50}^{0.75}), & D_{50} \geq 0.5 \text{ mm}, \end{cases} \quad (\text{B1})$$

262 such that with the inclusion of clay $L_{t\infty} = \pi g d_0^2 / 2B_\theta U_t^2$, $d_0 = \lambda_e/\alpha$ and B_θ and α are given by eqs.
 263 (8) and (9), giving $L_{t\infty}$ as

$$L_{t\infty} = \frac{\pi}{2(s-1)} \times \begin{cases} \frac{1}{0.21[B_\theta \alpha^{1.5}]} \left(\frac{\lambda_e^{1.5}}{D_{50}^{0.5}} \right), & D_{50} < 0.5 \text{ mm}, \\ \frac{1}{0.46\pi[B_\theta \alpha^{1.75}]} \left(\frac{\lambda_e^{1.75}}{D_{50}^{0.75}} \right), & D_{50} \geq 0.5 \text{ mm}, \end{cases} \quad (\text{B2})$$

264 and $AL_{t\infty}$ as $\lambda_e/0.142[\alpha]$ remains the same. Figure B1 shows the effect of this parameterisation of
 265 the threshold of motion for the first example case of Wu et al. (2018) depicted in Figures 2a,d.
 266 Unlike Figure 2d, the measured values of h and L are outside the range predicted for $C_0 = 7.4\%$.

267 **Acknowledgments**

268 The participation of JM, EMP, XW, RF, JHB and DRP was made possible thanks to funding by
 269 the European Research Council under the European Union's Horizon 2020 research and
 270 innovation program (grant no. 725955). Participation of RF was also supported by the
 271 Leverhulme Trust, Leverhulme Early Career Researcher Fellowship (grant ECF-2020-679).

272 **Open Research**

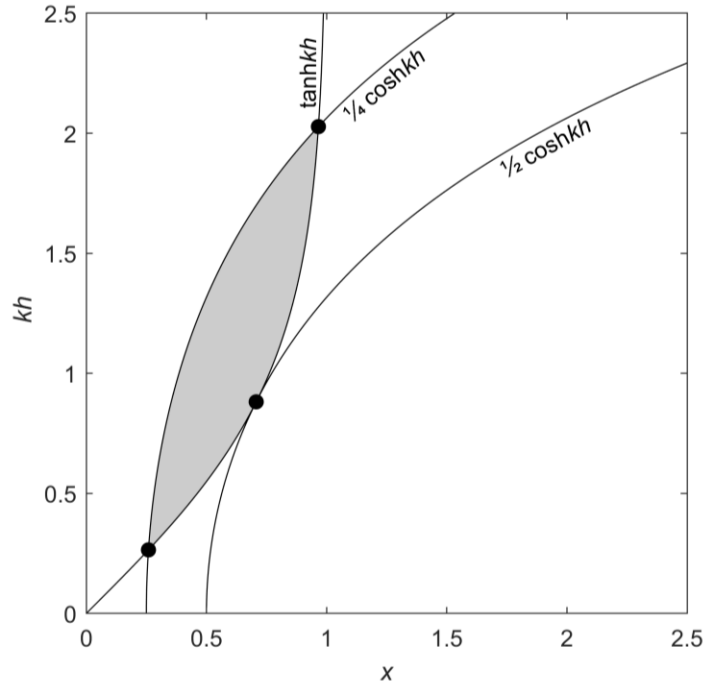
273 Eqs. (8) and (9) are from Wu et al. (2024), which has its own open-access policy.

274 **References**

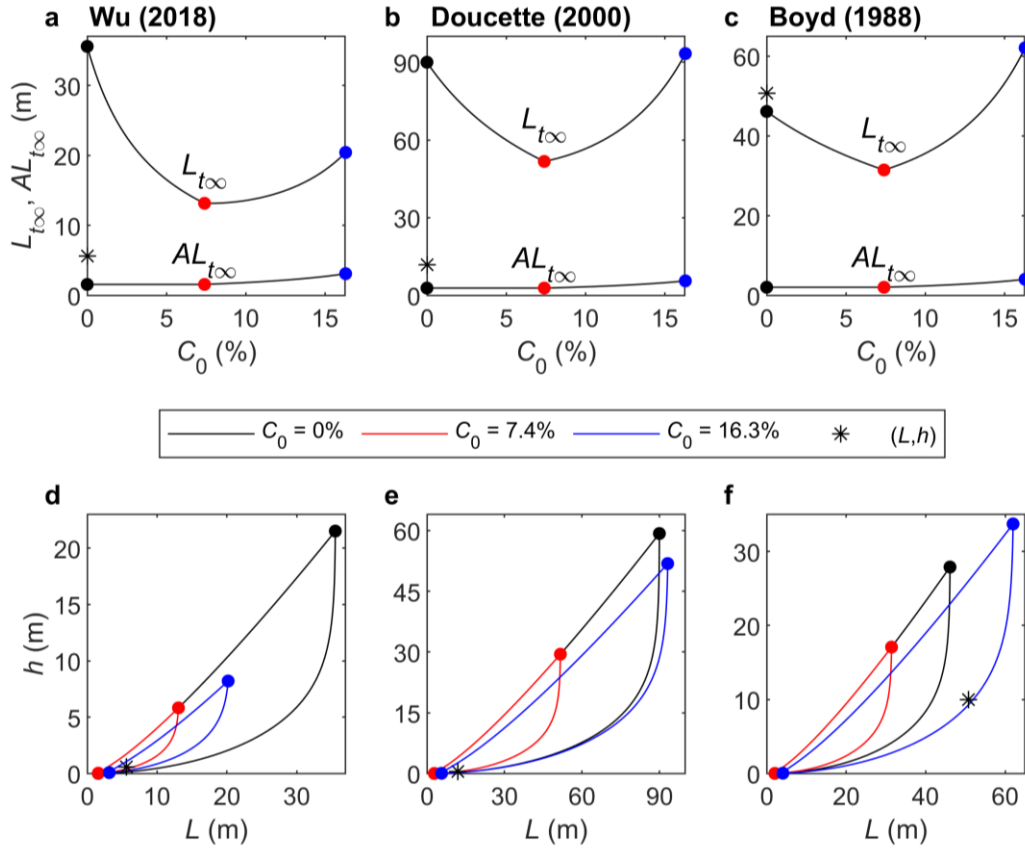
- 275 Allen, P.A. (1981). Some guidelines in reconstructing ancient sea conditions from wave
 276 ripplemarks. *Marine Geology*, 43, 59–67. [https://doi.org/10.1016/0025-3227\(81\)90176-6](https://doi.org/10.1016/0025-3227(81)90176-6)
- 277 Allen, P.A., & Hoffman, P.F. (2005). Extreme winds and waves in the aftermath of a
 278 Neoproterozoic glaciation. *Nature*, 433, 123–127. <https://doi.org/10.1038/nature03176>
- 279 Aspler, L.B., Chiarenzelli, J.R., & Bursey, T.L. (1994). Ripple marks in quartz arenites of the
 280 Hurwitz group, Northwest territories, Canada: evidence for sedimentation in a vast, early
 281 Proterozoic, shallow, fresh-water lake. *Journal of Sedimentary Research*, A64, 282–298.
 282 <https://doi.org/10.1306/D4267D7F-2B26-11D7-8648000102C1865D>
- 283 Baas, J.H. (1994). A flume study on the development and equilibrium morphology of current
 284 ripples in very fine sand. *Sedimentology*, 41, 185–209. <https://doi.org/10.1111/j.1365-3091.1994.tb01400.x>
- 285 Boyd, R., Forbes, D.L., & Heffler, D.E. (1988). Time-sequence observations of wave-formed
 286 sand ripples on an ocean shoreface. *Sedimentology*, 35, 449–464. <https://doi.org/10.1111/j.1365-3091.1988.tb00997.x>
- 287
 288
- 289 Collinson, J., & Mountney, N. (2019). *Sedimentary structures* (Fourth Edition), Edinburgh, UK:
 290 Dunedin Academic Press. ISBN 1780460627
- 291 Cuadrado, D.G. (2020). Geobiological model of ripple genesis and preservation in a heterolithic
 292 sedimentary sequence for a supratidal area. *Sedimentology*, 67, 2747–2763.
 293 <https://doi.org/10.1111/sed.12718>
- 294 Davies, N.S., Liu, A.G., Gibling, M.R., & Miller, R.F. (2016). Resolving MISS conceptions and
 295 misconceptions: A geological approach to sedimentary surface textures generated by microbial
 296 and abiotic processes. *Earth-Science Reviews*, 154, 210–246.
 297 <https://doi.org/10.1016/j.earscirev.2016.01.005>
- 298 Diem, B. (1985). Analytical method for estimating palaeowave climate and water depth from
 299 wave ripple marks. *Sedimentology*, 32, 705–720. <https://doi.org/10.1111/j.1365-3091.1985.tb00483.x>
- 300
 301 Doucette, J.S. (2000). The distribution of nearshore bedforms and effects on sand suspension on
 302 low-energy, micro-tidal beaches in Southwestern Australia. *Marine Geology*, 165, 41–61.
 303 [https://doi.org/10.1016/S0025-3227\(00\)00002-5](https://doi.org/10.1016/S0025-3227(00)00002-5)
- 304 Komar, P.D., & Miller, M.C. (1973). The threshold of sediment movement under oscillatory
 305 water waves. *Journal of Sedimentary Petrology*, 43, 1101–1110.
 306 <https://doi.org/10.1306/74D7290A-2B21-11D7-8648000102C1865D>
- 307 Lamb, M.P., Fischer, W.W., Raub, T.D., Perron, J.T., & Myrow, P.M. (2012). Origin of giant
 308 wave ripples in snowball Earth cap carbonate. *Geology*, 40, 827–830.
 309 <https://doi.org/10.1130/G33093.1>
- 310 Malarkey, J., Baas, J.H., Hope, J.A., Aspden, R.J., Parsons, D.R., Peakall, J., Paterson, D.M.,
 311 Schindler, R.J., Ye, L., Lichtman, I.D., Bass, S.J., Davies, A.G., Manning, A.J., & Thorne, P.D.
 312 (2015). The pervasive role of biological cohesion in bedform development. *Nature*
 313 *communications*, 6, 6257. <https://doi.org/10.1038/ncomms7257>
- 314 Malarkey, J., & Davies, A.G. (2003) A non-iterative procedure for the Wiberg and Harris (1994)
 315 oscillatory sand ripple predictor. *Journal of Coastal Research*, 19, 738–739.
 316 <http://www.jstor.org/stable/4299210>
- 317 Miche, R. (1944). Mouvements ondulatoires de la mer en profondeur constante ou décroissante.
 318 *Annales des Ponts et Chaussées*, 19, 369–406.
 319 <https://repository.tudelft.nl/islandora/object/uuid%3A6fceef55-d71b-4e3e-a94f-98ff17cb8f91>

- 320 Miller, M.C., & P.D. Komar (1980). Oscillation sand ripples generated by laboratory apparatus.
 321 *Journal of Sedimentary Petrology*, 50, 173–182. [https://doi.org/10.1306/212F799B-2B24-11D7-](https://doi.org/10.1306/212F799B-2B24-11D7-8648000102C1865D)
 322 [8648000102C1865D](https://doi.org/10.1306/212F799B-2B24-11D7-8648000102C1865D)
- 323 Mogridge, G.R., Davies, M.H., & Willis, D.H. (1994). Geometry prediction for wave-generated
 324 bedforms. *Coastal Engineering*, 22, 255–286. [https://doi.org/10.1016/0378-3839\(94\)90039-6](https://doi.org/10.1016/0378-3839(94)90039-6)
- 325 Parsons, D.R., Schindler, R.J., Hope, J.A., Malarkey, J., Baas, J.H., Peakall, J., Manning, A.J.,
 326 Ye, L., Simmons, S., Paterson, D.M., Aspden, R.J., Bass, S.J., Davies, A.G., Lichtman, I.D., &
 327 Thorne, P.D. (2016). The role of biophysical cohesion on subaqueous bed form size.
 328 *Geophysical Research Letters*, 43, 1566–1573. <https://doi.org/10.1002/2016GL067667>
- 329 Pedocchi, F., & García, M.H. (2009). Ripple morphology under oscillatory flow: 2. Experiments,
 330 *Journal of Geophysical Research*, 114, C12015. <https://doi.org/10.1029/2009JC005356>
- 331 Perron, J.T., Myrow, P.M., Huppert, K.L., Koss, A.R., & Wickert, A.D. (2018). Ancient record
 332 of changing flows from wave ripple defects. *Geology*, 46, 875–878.
 333 <https://doi.org/10.1130/G45463.1>
- 334 Pochat, S., & Van Den Driessche, J. (2011). Filling sequence in Late Paleozoic continental
 335 basins: A chimera of climate change? A new light shed given by the Graissessac–Lodève basin
 336 (SE France). *Palaeogeography, Palaeoclimatology, Palaeoecology*, 302, 170–186.
 337 <https://doi.org/10.1016/j.palaeo.2011.01.006>
- 338 Sleath, J.F.A. (1975). A contribution to the study of vortex ripples. *Journal of Hydraulic*
 339 *Research*, 13, 315–328. <https://doi.org/10.1080/00221687509499705>
- 340 Soulsby, R. (1997). *Dynamics of Marine Sands: A Manual for Practical Applications*, London
 341 UK: Thomas Telford. ISBN 072772584X
- 342 Soulsby, R.L., Hamm, L., Klopman, G., Myrhaug, D., Simons, R.R., & Thomas, G.P. (1993).
 343 Wave–current interactions within and outside the bottom boundary layer. *Coastal Engineering*,
 344 21, 41–69. [https://doi.org/10.1016/0378-3839\(93\)90045-A](https://doi.org/10.1016/0378-3839(93)90045-A)
- 345 Vignaga, E., Sloan, D.M., Luo, X., Haynes, H., Phoenix, V.R., & Sloan, W.T. (2013). Erosion of
 346 biofilm-bound fluvial sediments. *Nature Geoscience*, 6, 770–774.
 347 <https://doi.org/10.1038/ngeo1891>
- 348 Wetzel, A., Allenbach, R., & Allia, V. (2003). Reactivated basement structures affecting the
 349 sedimentary facies in a tectonically “quiescent” epicontinental basin: an example from NW
 350 Switzerland. *Sedimentary Geology*, 157, 153–172. [https://doi.org/10.1016/S0037-](https://doi.org/10.1016/S0037-0738(02)00230-0)
 351 [0738\(02\)00230-0](https://doi.org/10.1016/S0037-0738(02)00230-0)
- 352 Whitehouse, R., Soulsby, R., Roberts W., & Mitchener, H. (2000). *Dynamics of estuarine muds:*
 353 *A Manual for Practical Applications*, London UK: Thomas Telford. ISBN 0727728644
- 354 Wiberg, P.L., & Harris, C.K. (1994). Ripple geometry in wave-dominated environments. *Journal*
 355 *of Geophysical Research*, 99(C1), 775–789. <https://doi.org/10.1029/93JC02726>
- 356 Wu, X., Baas, J.H., Parsons, D.R., Eggenhuisen, J., Amoudry, L., Cartigny, M., McLelland, S.,
 357 Mouazé, D., & Ruessink, G. (2018). Wave ripple development on mixed clay–sand substrates:
 358 Effects of clay winnowing and armoring. *Journal of Geophysical Research: Earth Surface*, 123,
 359 2784–2801. <https://doi.org/10.1029/2018JF004681>
- 360 Wu, X., Fernández, R., Baas, J.H., Malarkey, J., & Parsons, D.R. (2022). Discontinuity in
 361 equilibrium wave–current ripple size and shape and deep cleaning associated with cohesive
 362 sand–clay beds. *Journal of Geophysical Research: Earth Surface*, 127, e2022JF006771.
 363 <https://doi.org/10.1029/2022JF006771>

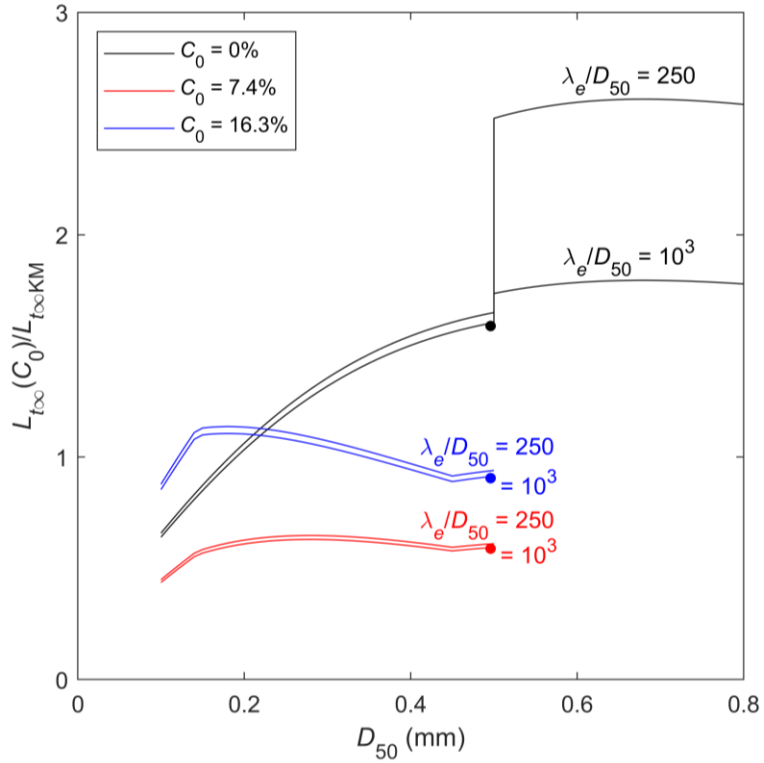
364 Wu, X., Malarkey, J., Fernández, R., Baas, J.H., Pollard, E., & Parsons, D.R. (2024). Influence
365 of cohesive clay on wave-current ripple dynamics captured in a 3D phase diagram. *Earth Surface*
366 *Dynamics*, 12, 231–247. <https://doi.org/10.5194/esurf-12-231-2024>



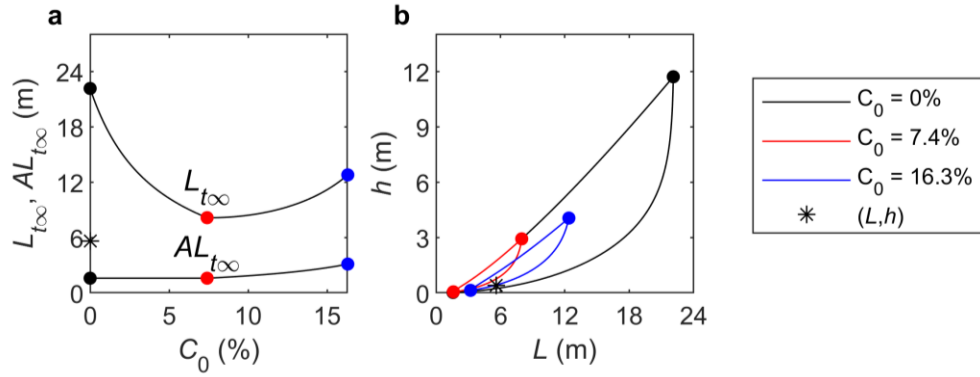
367 **Figure 1** kh versus x (L/L_{∞}) for the limiting case of $A = 1/2$ and also $A = 1/4$. Dots correspond to x
 368 $= 2^{-1/2}$ and $kh = \operatorname{arctanh} 2^{-1/2}$, for $A = 1/2$; $x_{\max, \min} = 1/2(2 \pm 3^{1/2})^{1/2}$ and $kh_{\max, \min} = \operatorname{arctanh}[x_{\max, \min}]$, for A
 369 $= 1/4$, and shading represents allowable values of x and kh for $A = 1/4$ ($1/4 \cosh kh \leq x \leq \tanh kh$).



370 **Figure 2** (a,b,c) Threshold, $L_{t\infty}$, and wave-breaking, $AL_{t\infty}$, scales, eqs. (10b,c), versus C_0 and
 371 (d,e,f) L - h phase space from eq. (5), showing the different ranges for $C_0 = 0, 7.4$ and 16.3% and
 372 the measured L and h . For (a,d) Wu et al. (2018), $\lambda_e = 278D_{50}$, $D_{50} = 0.496$ mm, $\theta_0 = 0.032$, $L =$
 373 5.62 m and $h = 0.6$ m; for (b,e) Doucette (2000), $\lambda_e = 250$ mm, $D_{50} = 0.22$ mm, $\theta_0 = 0.045$, $L =$
 374 11.9 m and $h = 0.47$ m, and for (c,f) Boyd et al. (1988), $\lambda_e = 180$ mm, $D_{50} = 0.11$ mm, $\theta_0 = 0.076$,
 375 $L = 50.7$ m and $h = 10$ m. Legend applies to d,e,f; colours in a,b,c are consistent with the legend.



376 **Figure 3** Relative size of $L_{t\infty}(C_0)$ from eq. (10b) normalised by the clean-sand $L_{t\infty}$ from eq. (B2),
 377 $L_{t\infty KM}$, for $C_0 = 0, 7.4$ and 16.3% . $\lambda_e/D_{50} = 250$ and 1000 , and the dots correspond to Wu et al.'s
 378 (2018) clean-sand experiment in Figure 2a.



379 **Figure B1** (a) Threshold, $L_{t\infty}$, and wave-breaking scales, $AL_{t\infty}$, eqs. (B2) and (10c), versus C_0 and
 380 (b) $L-h$ phase space from eq. (5) showing the different ranges for $C_0 = 0, 7.4$ and 16.3% and the
 381 measured h and L for Wu et al. (2018), $\lambda_e = 278D_{50}$, $D_{50} = 0.496$ mm, $h = 0.6$ m and $L = 5.62$ m.